IEEE Access
Multidisciplinary | Rapid Review | Open Access Journal

Received January 29, 2019, accepted February 25, 2019, date of publication March 14, 2019, date of current version March 26, 2019.

Digital Object Identifier 10.1109/ACCESS.2019.2902562

Phase-Based Nonrigid Deformation for Digital Subtraction Angiography

SOOCHAHN LEE[1], CHANG HO JEON[2], LEONARD SUNWOO[3], DONG YUL OH[3], AND KYONG JOON LEE[3]

[1]School of Electrical Engineering, Kookmin University, Seoul 02707, South Korea
[2]Department of Radiology, Pusan National University Hospital, Busan 46241, South Korea
[3]Department of Radiology, Seoul National University Bundang Hospital, Seongnam 13620, South Korea

Corresponding author: Kyong Joon Lee (kjoon@snubh.org)

This work was supported in part by the National Research Foundation of South Korea (NRF) through the Ministry of Education under Grant 2017R1D1A1B03033610, and in part by the Interdisciplinary Research Initiatives Program through the College of Engineering and the College of Medicine, Seoul National University, under Grant 800-20170169.

ABSTRACT We present a method for digital subtraction angiography based on phase-based nonrigid deformation with specific consideration for changes between the image pairs. Input images are transformed into a scale-space representation using complex-valued filter responses. We apply a novel selection criterion to discern object motion and actual change by comparing the magnitudes in the responses. By manipulating phase, we directly generate a deformed image without explicit calculation of motion vectors. Our method is particularly useful in angiographic imaging where subtle changes between the image pairs should be preserved within the deformation and subtraction process. The experiments show that the proposed method preserves contrast for vessels and tumor stains while reducing motion artifact, which is clinically meaningful.

INDEX TERMS Image registration, change detection, biomedical imaging, angiography.

I. INTRODUCTION

Angiography is a fluoroscopic technique to visualize the patient's blood vessels by injecting radiopaque contrast medium into the vessels which are normally invisible in plain radiography images. It is widely used in interventional procedures identifying vascular abnormalities, detecting injury to arteries after trauma, or evaluating arteries feeding a tumor prior to surgeries. Digital Subtraction Angiography (DSA) is where a pre-contrast image (called *mask* image) taken before the injection is subtracted from the contrast image (called *live* image) to enhance the visibility of the vessel. Given that the live and mask image pairs are acquired at different points in time, a simple subtraction strategy may yield undesirable artifacts due to patient motion. While nonrigid registration is often applied before subtraction, it can have trouble distinguishing changes in the image due to motion and changes due to injection of contrast medium. This may lead to the reduction of desirable contrast from the visualized vessels or unsatisfactory reduction of motion artifacts.

A. RELATED WORK

An early method for motion compensation in DSA, *pixel-shift* [4], tracks a region in the mask image and compensates the motion by panning the whole live image. It has been widely adopted in commercial products for its simplicity but is limited to addressing rigid body motion only.

To this end, Meijering *et al.* [5] introduced a new method to handle the nonrigid motion between the mask and live images. The method extracts feature points in both images and matches the features to find correspondences. In [6], Nejati *et al.* follow the feature-based approach employing the multi-level b-spline to cover the artifacts from larger displacements. The method is further improved by modeling of intensity variation in [26]. Liu *et al.* [25] presents a spatial rotating coordinate system designed to eliminate the incorrect feature points. In contrast to the *sparse* feature-matching methods, an image-based approach obtaining dense correspondence was proposed in [7]. This technique produces highly accurate registration results but is not practically applicable due to its heavy computational complexity. Since those nonrigid approaches generally assume uniquely matching points, they may fail to find correspondences for newly visible vessels (by the contrast medium) in the live image. Several methods [6], [8] carefully select features that are independent of the vessel region or exclude the vessel region in the registration process. This step usually requires manual interaction of qualified experts.

An energy subtraction angiography [22], [23] can handle motion artifact as well, which employs a dual-energy

The associate editor coordinating the review of this manuscript and approving it for publication was Tao Zhou.

X-ray source to capture two consecutive frames with different energy level within a very short time. However, they inherently suffer from low contrast of the resulting DSA due to the insufficient energy gap between vessels and background tissues. A recent method [27] introduced respiratory synchronization to implement fast and accurate compensation for a real-time solution, but it has difficulty dealing with motions stemming from unintended factors, such as heartbeat or bowel movement. Moreover, those methods require special hardware to generate fast kV switching or to match the respiratory phase of the patient and thus are not applicable to the general DSA system.

There have been many works on change detection in images. We refer the interested reader to the systematic review in [1], introducing various strategies with robust registration as a critical preprocessing step. One approach to jointly solve the image registration and change detection is optical flow estimation with occlusion handling [3]. An up-to-date method [21] presents a novel occlusion detection criterion, which does not critically depend on a precomputed dense motion flow field. Hur and Roth [20] recently proposed to utilize symmetry properties of the flow and occlusion; i.e., the forward-backward consistency and occlusion-disocclusion symmetry in the energy function. Wang *et al.* [19] adopted unsupervised learning for explicit occlusion modeling and introduced a new warping approach to accelerate training of significant motion. Although these approaches yield state-of-the-art accuracy for dense correspondence field (even for the occluded region,) handling the fluoroscopic images can be a different problem, where the occluding objects are generally partially opaque and are often close to transparent.

B. OUR APPROACH

We thus propose a new method for DSA to inherently detect and isolate changes between the images within a framework for nonrigid image alignment. Inspired by the work of [9] and [10], we also model the motion of individual pixels as a phase shift in the frequency domain. Within this framework, aligning the source pixel phase with the target can synthesize a deformed target image, without explicit computation of motion vectors. To this end, input images are first transformed into the frequency domain. Multi-scale local representations are generated with complex steerable pyramid filters [11], yielding phase and magnitude images with various orientations at each level of scale. Within this domain, we essentially detect regions with newly visible vessels based on magnitude. Our assumption is that regions common in both images, where motions have occurred, will have similar magnitudes but shifts in phase. For these regions, we compensate for the motion by adjusting the phase difference. In contrast, for regions with newly visible vessels, the actual appearance change will cause the magnitudes to be different. For these regions, we leave the phase unchanged. Based on the adaptively manipulated phases with the original magnitudes, a deformed image is reconstructed. The vessels are visually enhanced by subtracting the deformed image from the target image. Compared to the other state-of-the-art registration methods, the proposed method shows reduced motion artifact while better preservation of the vessels.

We note that some previous approaches also employ the local frequency information for image registration process [12], [13], but as a part of matching criteria to obtain the explicit motion vectors, due of its invariance to image modality. Since they do not assume changes between images, they are not suitable for DSA.

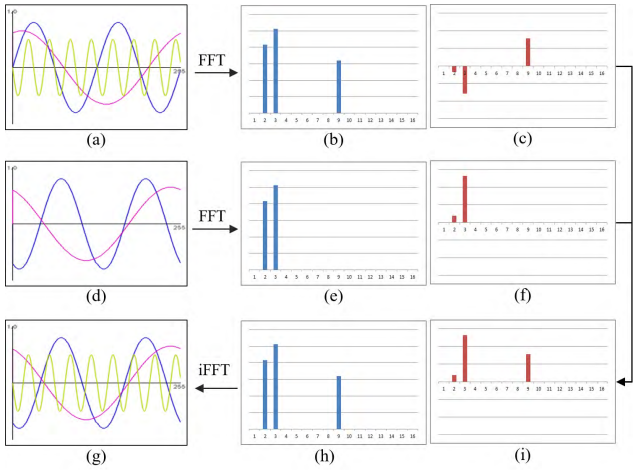

FIGURE 1. 1-D toy example to conceptually explain the proposed method. (a) Reference image. (b) Magnitude and (c) phase spectrums obtained by applying DFT to the reference image. (d) Target image. (e) Magnitude and (f) phase applying DFT to the target image. (h) Magnitude for the deformed image, copied from (b). (i) Phase for the deformed image, which is determined by comparing the magnitude of the reference (b) and that of the target (e) for each frequency. (g) Deformed image applying iDFT to (h) and (i).

II. METHOD

A. DISCERNING CHANGES USING PHASE AND MAGNITUDE: A CONCEPT

We start with a conceptual toy example. Assume an 1-D reference image $I(x)$ comprising three sinusoidal signals shown in Fig. 1(a), $S_k(x) = A_k \sin(\omega_k(x - \Phi_k))$, where A_k, $k \in \{1, 2, 3\}$ with $\omega_1 < \omega_2 < \omega_3$. Likewise, a corresponding target image can be defined as $J(x) = \sum_{k=1}^{3} B_k \sin(\omega_k(x - \Delta_k))$. We consider S_1 and S_2 as individual objects that have moved in different direction by amount of $\Phi_1 - \Delta_1$ and $\Phi_2 - \Delta_2$ respectively. Note we set $B_3 = 0$ and the target image (Fig. 1(d)) contains only two sinusoids. The sinusoid S_3 can be considered as the actual difference which is only shown in the reference image. Our goal is to construct a deformed reference image defined by $I'(x) = \sum_{k=1}^{3} A'_k \sin(\omega_k(x - \Phi'_k))$. Initially we set $I'(x) = I(x)$, thus $\forall k, A'_k = A_k$ and $\Phi'_k = \Phi_k$.

In the first step, the images are transformed into the frequency domain. Fig. 1(b), (c), (e), and (f) illustrate the magnitude and phase information of both signals resulting from Discrete Fourier Transform (DFT.) Next, we walk through the discrete frequency domain and compare the magnitudes of

the reference and the target images. We assume the similar magnitudes in the frequency domain indicate the identical signals in the original domain. In this case object motion can be compensated by adjusting the phase; we may simply set those phases of the deformed image identical to the phases of the target, such that $\Phi'_1 = \Delta_1$ and $\Phi'_2 = \Delta_2$. In contrast, the magnitude A_3 of the reference will be significantly larger than that of the target ($B_3 = 0$) for the actual difference signal S_3, and in this case we set the phase of the deformed image to stay unchanged. Finally we reconstruct the deformed image by applying the inverse Fourier transform, as shown in Fig. 1(g). The algorithm can be easily extended to a general signal represented by a sum of complex sinusoids, $I(x) = \sum_{-\infty}^{\infty} A_\omega e^{i\omega x}$.

B. EXTENSION TO 2-D NONRIGID MOTION USING STEERABLE PYRAMID

While the signals comprising sinusoids in the above example can readily be interpreted through their frequency spectrums computed by the *global* Fourier transform, this is obviously not the case for 2-D medical images. For real images, both the source and target images have different locally varying appearances, and thus locally different frequency components. For the same principle as the example mentioned above to be applicable, we need to obtain localized frequency analyses for each local region. Furthermore, since images are in 2-D, the orientation of the frequency components can also be considered to compare the source and target images in more detail.

We thus employ the complex steerable pyramid [11], which provides frequency analyses that are localized in terms of both translation and orientation. It has shown good results in applications such as motion magnification [9], [14] and image interpolation [10]. To build the pyramid, a set of scalable filters with orientation, $\Psi_{\omega,\theta}$ are applied to yield a complex-valued response $R_{\omega,\theta}$ on the spatial domain for frequency ω and orientation θ; that is, $R_{\omega,\theta} = (I * \Psi_{\omega,\theta})(x, y) = C_{\omega,\theta}(x, y) + iS_{\omega,\theta}(x, y)$. Here, the frequency spectrum $R_{\omega,\theta}$ is the frequency spectrum of the local image appearance at spatial coordinate (x, y), for the frequency and orientation bands centered at ω and θ. Also, $C_{\omega,\theta}$ and $S_{\omega,\theta}$ denotes the real and imaginary parts of the response.

If we assume N_ω frequency bands and N_θ, a total of $N_\omega \times N_\theta$ convolutions must be performed on the whole image to compute the steerable pyramid. This can be computed more efficiently by first transforming the image and the filters $\Psi_{\omega,\theta}$ into the frequency domain. Then, by applying the convolution theorem $\mathcal{F}(I * \Psi_{\omega,\theta}) = \mathcal{F}(I) \cdot \mathcal{F}(\Psi_{\omega,\theta})$, where $\mathcal{F}$ denotes the DFT, we can replace convolution with multiplication. Here, DFTs of filter responses decompose DFT of the image into a set of oriented subbands in the frequency domain. Fig. 2 shows an example of efficiently building the steerable pyramid using the convolution theorem. Since the subbands constitute a "tight" frame [11], the original image can be reconstructed from aggregation of the subbands (Fig. 2 (d)) using inverse DFT.

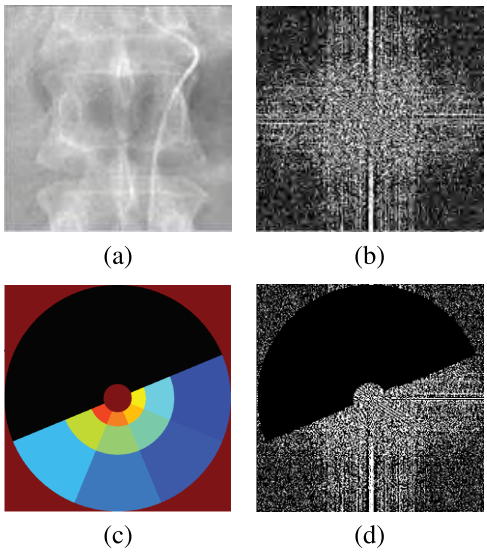

FIGURE 2. Efficient computation of steerable pyramid. (a) Original input image. (b) DFT of the input image (the real part). (c) DFT of steerable pyramid filters. Each subband represents a filter and is illustrated with different colors [9]. (d) Aggregation of filter responses. Each response can be easily calculated by multiplying corresponding subband to the DFT of input image. Applying inverse DFT to the aggregation can reconstruct the original image.

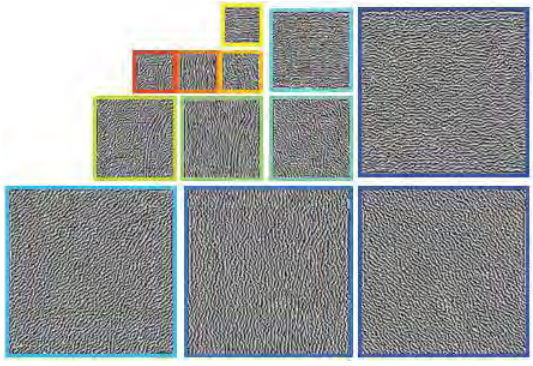

FIGURE 3. Visualization of the steerable pyramid, of phases, for the sample input image of Fig. 2. The border color for each level corresponds to the color of the subband in Fig. 2 (c). We build a pair of pyramids, corresponding to magnitude and phase from the input image, and generate the corresponding filter response R^{def} for the deformed image by combining magnitude and phase that are defined by the proposed algorithm.

C. ALGORITHM DETAILS OF PROPOSED METHOD

We build a pair of complex steerable pyramids from a reference image I^{ref} and a target image I^{tar}, producing two sets of complex-valued filter responses $R^{ref}_{\omega,\theta}$ and $R^{tar}_{\omega,\theta}$. It is straightforward to compute magnitude $A_{\omega,\theta}(x, y) = \sqrt{C_{\omega,\theta}(x, y)^2 + S_{\omega,\theta}(x, y)^2}$ and phase $\Phi_{\omega,\theta}(x, y) = \arctan(S_{\omega,\theta}(x, y)/C_{\omega,\theta}(x, y))$ from the responses. Fig. 3 demonstrates the pyramid of phases for an input image. The boundary color for each phase corresponds to the color of subbands in Fig. 2 (c).

For each response, we can generate the corresponding filter response R^{def} for deformed image by combining magnitude

and phase that are defined by,

$$A^{def}_{\omega,\theta}(x,y) = A^{ref}_{\omega,\theta}(x,y) \tag{1}$$

$$\Phi^{def}_{\omega,\theta}(x,y) = \begin{cases} \Phi^{ref}_{\omega,\theta}(x,y), & \text{if } A^{tar}_{\omega,\theta}(x,y) < \beta A^{ref}_{\omega,\theta}(x,y) \\ \Phi^{tar}_{\omega,\theta}(x,y), & \text{otherwise} \end{cases} \tag{2}$$

where β is a parameter controlling the similarity comparison constraint, with the range of $0 < \beta < 1$. If β is close to 0, only significant magnitude differences are considered as actual changes. In the opposite case that β is close to 1, most of changes are considered as object motion.

The proposed algorithm can be summarized as follows:

1) For input reference image I^{ref} and a target image I^{tar}, build a complex steerable pyramid pair to yield a set of filter response pairs $R^{ref}_{\omega,\theta}$ and $R^{tar}_{\omega,\theta}$, for all possible values of ω and θ.
2) Compute magnitudes $A^{ref}_{\omega,\theta}$, $A^{tar}_{\omega,\theta}$ and phases $\Phi^{ref}_{\omega,\theta}$, $\Phi^{tar}_{\omega,\theta}$ from $R^{ref}_{\omega,\theta}$ and $R^{tar}_{\omega,\theta}$.
3) Generate the magnitude $A^{def}_{\omega,\theta}$ and phase $\Phi^{def}_{\omega,\theta}$ according to the Eq. (1) and (2) to compute a filter response for a deformed image.
4) Reconstruct the deformed image I^{def} from $A^{def}_{\omega,\theta}$ and $\Phi^{def}_{\omega,\theta}$.
5) Compute subtracted image $I^{sub} = I^{tar} - I^{def}$.

III. EXPERIMENTAL RESULTS

A. DATASET

We validate our motion compensation method on 16 image sets captured with interventional angiography machines (AXIOM Artis; Siemens Medical Solutions, Malvern, PA) in 2016 in Seoul National University Bundang Hospital. Each image set contains 20–200 images. The institutional review board waived informed consent due to the retrospective study design and the use of anonymized patient data. The image sets contain various clinical cases such as transarterial chemoembolization (TACE), adrenal venography, angioplasty for hemodialysis arteriovenous fistula, and bronchial artery embolization.

All the images are resized to 512×512 pixels. Both the number of orientations and the number of levels in a steerable pyramid are set to six. The scale factor between the levels is set to two. More levels and orientations hardly improve registration accuracy in our experiments but require more computational complexity. All the experiments are executed on a system with 3.30Ghz Intel Core i5 CPU. For the difference criteria comparing magnitudes, we set $\beta = 0.1$.

B. COMPARATIVE METHODS

We compare the proposed approach with two methods [6], [7] recently showing excellent results in DSA motion correction. A method designed for accurate optic flow estimation [3] is also included, which presents a highly competitive performance, particularly for occlusion detection. Other recent methods [23], [27] are excluded since they only accept images from special devices such as dual energy X-ray or respiratory phase matching, which is not comparable to our method dealing with common images from generic hardware.

The first method for comparison [6] utilizes the multilevel B-spline (MBS) with the Free Form Deformation (FFD) [15], that is defined on a uniform mesh of control points. An optimal deformation is then determined that balances the alignment of local features of the source image to the target image and the cost of deforming the uniform mesh. The second method for comparison [7] is based on the Markov Random Field (MRF), a graphical model, where an energy function is defined on constituent vertices subsets immediately connected by edges. Most often two types of potentials are defined: The data term measures similarity of local appearance and the smoothness term measures similarity of displacement neighboring vertices. The negative log likelihood of these potentials results in a cost function along with a scalar balancing parameter λ and is optimized by an iterative energy minimization strategy. The third method for comparison [3] also follows this approach for the cost function, but it proposes a more elaborated data term extending the coarse-to-fine scheme to handle motion detail of fine structures, gradually addressing occlusion in each scale. Our implementation of the comparative methods are built on the publicly available softwares [17], [18] and the program code provided by the authors.

C. QUALITATIVE COMPARISON

To the best of our knowledge, a standard quantitative measure for assessing the quality of DSA images does not exist. An angiographic change should be noticed and evaluated by an actual human user in a clinical environment, but it is challenging to create the ground-truth map for the angiographic change and also to define how well the change is noticed. Thus, we first evaluate the performance in a qualitative manner.

In Fig. 4, we show (a) live and (b) mask images used for TACE, along with subtraction images (c) w/o motion compensation, and with motion compensation using (d) MBS [6], (e, f) MRF [7] with varying λ, (g) motion-detail preserving (MDP) optical flow method [3] and (h) the proposed method. The images contain small motion of organs due to the patient's respiration together with the actual appearance change due to the contrast medium injection. Note the live image contains a faint tumor stain, indicated by the red box in (a), and shown more clearly in Fig 5. Localizing this region is clinically very important, and it should be more obviously recognized in DSA results. For the results of MBS (d), we see the dark tumor is indeed visible. But the various noise surrounding the tumor due to the errors in registration and the sparse control points may interfere with the observer noticing the tumor. The result from MRF (e) significantly reduces the motion artifact with the emphasis on flexibility of the registration ($\lambda = 0.1$), but it also reduces contrast for the clinically important tumor stain as well as the small vessels. This may stem from the fact that the technique tries to find the best

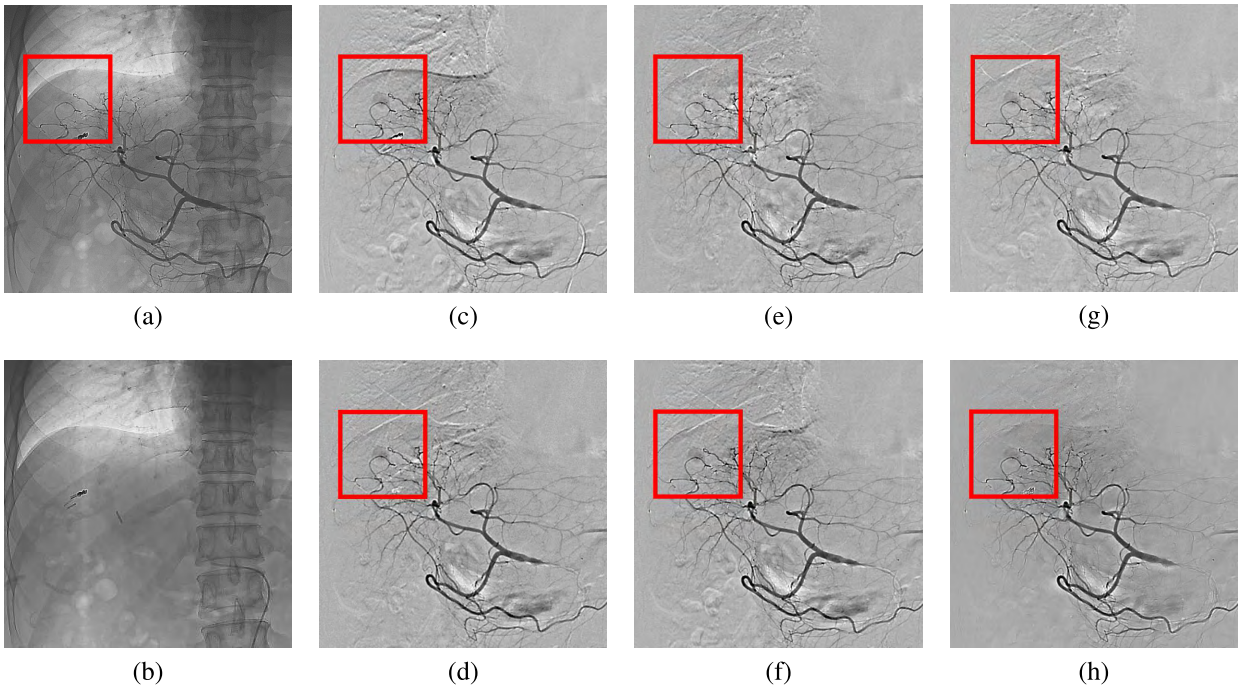

FIGURE 4. DSA results for TACE. (a) Live image with contrasted vessel. A tumor is also faintly stained by contrast medium, indicated in the red box. (b) Mask image. (c) DSA without motion compensation. (d) DSA with MBS [6] ($\lambda = 0.1$). (e) DSA with MRF [7] ($\lambda = 0.1$). (f) DSA with MRF [7] ($\lambda = 1.0$). (g) DSA with MDP [3]. (h) DSA with the proposed method. Best viewed electronically.

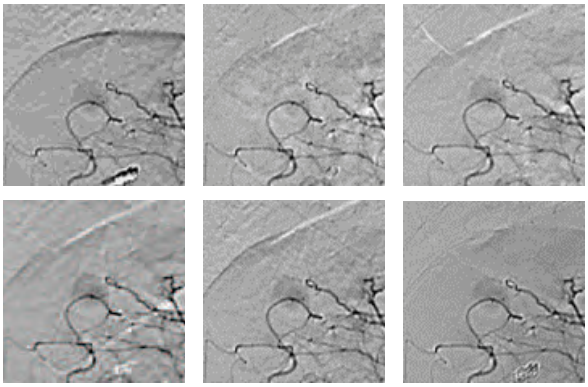

FIGURE 5. The respective zoomed views of Fig 4 (c,d,e,f,g,h) for the region in the red box of Fig 4 (a). The faint tumor stain can be seen in the image center. (upper left) without motion compensation, significant artifact stemming from lung motion is presented (the black arc-line over the stain.) The artifact from a marker seems obvious as well. (the white object under the vessels). (lower left) MBS result. The artifacts are reduced, but the various noise including the Gaussian blur may interfere with the observer noticing the tumor. (upper middle) MRF result with $\lambda = 0.1$ shows significantly reduced the motion artifact with the emphasis on flexibility of the registration but also presents reduced contrast for the clinically important tumor stain as well as the small vessels. (lower middle) MRF result with $\lambda = 1.0$. We may better recognize the tumor stain, but the artifacts caused by lung motion become vivid as a trade-off effect. (upper right) MDP result also suffers from the trade-off effect. (lower left) proposed method result successfully preserves the contrast for the tumor stain while greatly reducing the motion artifact.

corresponding pixel in the target live image for every pixel in the mask, including ones that are actually occluded, i.e., the vessel and the tumor stain. Depending on the sufficiency of pixel intensity contrast from the contrast agent, the contrasted regions may be incorrectly registered to similar regions, actually making the subtraction more vague in the result. With a different parameter reducing flexibility ($\lambda = 1.0$), we may better recognize the tumor stain in Fig. 4(f) but the artifacts caused by lung motion become vivid as a trade-off effect. The result of MDP (g) shows slightly less artifact than (f) by controlling the balancing parameter, but it also suffers from the tradeoff effect showing slightly less contrast than (f). In contrast, the proposed method (h) successfully preserves the contrast for the tumor stain while significantly reducing the motion artifact, as seen in the figures.

Experimental results in cases with tumor stains are demonstrated in Fig. 6 to highlight the clinical usefulness of the proposed method. We show (a) the live images along with DSA results (b) without motion compensation, (c) with MBS, (d) with MRF ($\lambda = 0.1$) and (e) with the proposed method. Each couple of rows shows results of different cases. The tumor stains are indicated in the red boxes on the live images in the leftmost position of the upper row. The whole frames shown in the upper rows and the zoomed tumor boxes are shown on the bottom. The first case, shown in the top two rows presents a case with a relatively large and conspicuous tumor observed even in the live image. The proposed method enhances the contrast and effectively removes the overall motion artifacts. For the second case, shown in the third and fourth rows, the tumors are relatively faint or small and thus difficult to delineate. In this case, noise resulting from motion may generate more contrast for the tumors as in the result without motion compensation of the second row case. While our method may show slightly lower contrast, the clarity

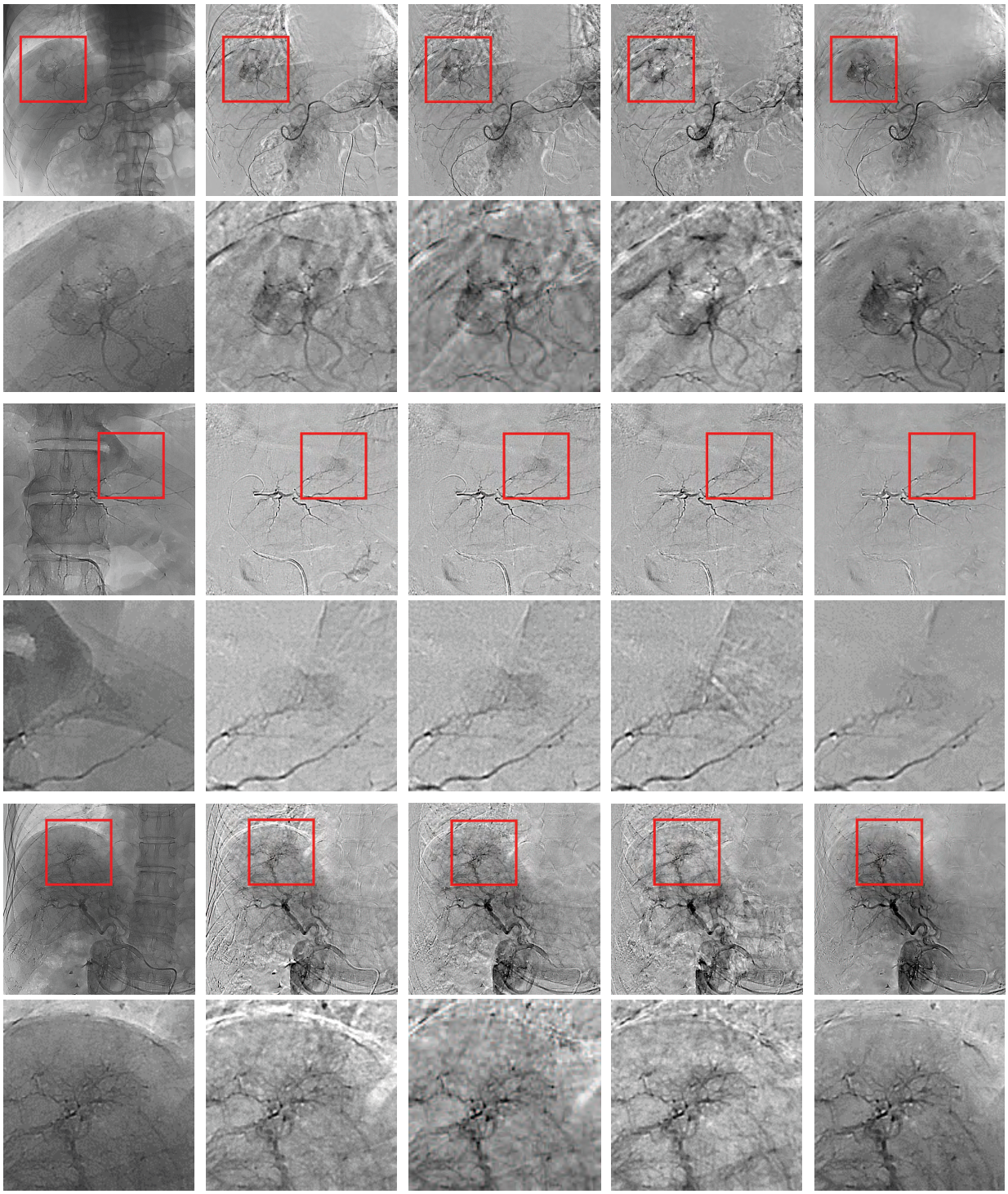

FIGURE 6. From left column: (a) live images, (b) DSA without motion compensation, (c) DSA with MBS, (d) DSA with MRF ($\lambda = 0.1$), and (e) DSA with the proposed method. From top row: each consecutive two rows represent different cases, where among the two the top row shows the whole image and the bottom row shows the zoomed view of the red box, containing a stained tumor, in the live image above. The proposed method enhances the contrast, especially for the stained tumor, and also effectively reduces the overall motion artifacts. Best viewed electronically.

of the boundary is improved due to the reduced noise. The bottom two rows show a case with complex structures including the lung and the ribs, which cause considerable motion artifacts. Our method is very effective in reducing the motion artifacts, again resulting in slightly weakened tumor contrast but clarified tumor boundary.

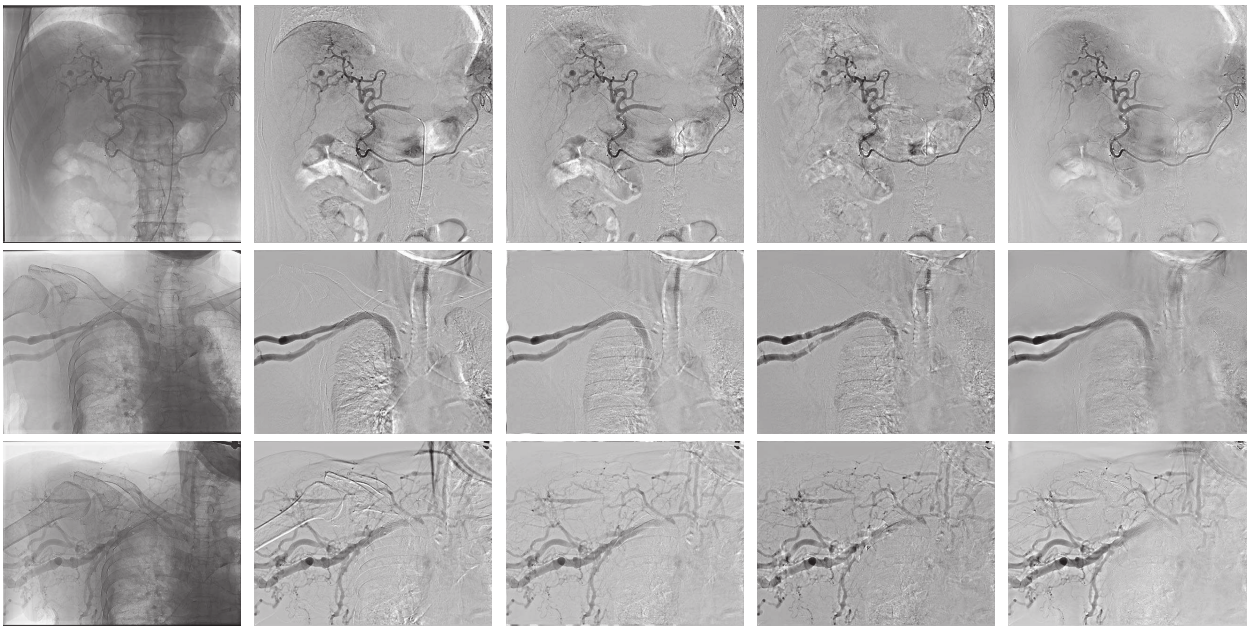

FIGURE 7. From left column: (a) live images, (b) DSA without motion compensation, (c) DSA with MBS, (d) MRF ($\lambda = 0.1$), and (e) DSA with the proposed method. The proposed method enhances the contrast and effectively removes the overall motion artifacts.

Further experimental results in cases with large motion between frames due to the respiratory motion of the lungs are shown in Fig. 7. We can see that the proposed method shows the least amount of artifacts in the regions without contrast agents, indicating the most accurate registration. We can also see from the results of the proposed method, that regions with contrast agent have high contrast, with clear delineation. This indicates that the proposed method is successful in only applying registration to the appropriate regions.

D. QUANTITATIVE COMPARISON

Although standard quantitative measures do not exist for an assessment of the quality of DSA images, we evaluate our method with Peak Signal-to-Noise Ratio (PSNR) and Contrast-to-Noise Ratio (CNR) with a specific definition of the foreground and background regions. We design the PSNR as a metric for image alignment and the CNR as a metric for change detection, respectively. The PSNR and CNR calculations employ the following definitions:

$$PSNR = 20\log_{10}\left(\frac{MAX_I}{MSE_{bg}}\right) \tag{3}$$

$$CNR = 20\log_{10}\left(\frac{|m_{fg} - m_{bg}|}{\sigma_{bg}}\right) \tag{4}$$

where MAX_I is the maximum possible pixel intensity ($= 4096$) and MSE_{bg} stands for mean squared error for background region. Note that the foreground is excluded in calculating MSE since the intended contrast should not be counted as a registration error. m_{fg} and m_{bg} indicate the means of intensities for foreground and background regions respectively, while σ_{bg} is the standard deviation for background.

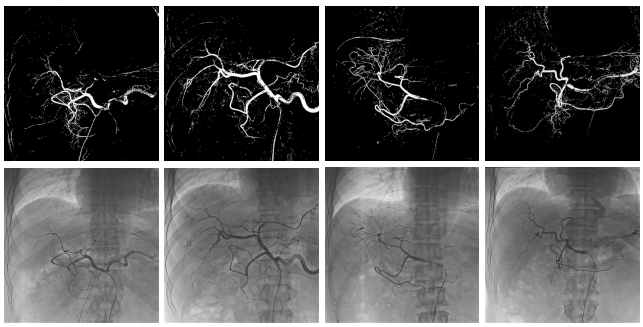

FIGURE 8. (Top row) Foreground (contrasted region, e.g., vessel) segmentation maps. (Bottom row) Live images presenting the contrasted region. We segment the region by simply thresholding the intensity of the DSA image without motion compensation. The resulting foreground approximately contains important vessel structures as seen. The erroneous non-foreground spots are negligible compared to the whole image size.

We consider the foreground as the region that is only visible in the live image due to contrast media (e.g., vessels and tumor stains.) To delineate the foreground region, we apply simple intensity thresholding to the DSA image without motion compensation. The resulting foreground approximately contains important vessel structures as illustrated in figure 3. Although the foreground determined by this simple approach will likely include erroneous non-foreground regions due to the lack of motion compensation, the relative amount of these errors will most likely be negligible compared to the whole image size.

The image sets generally contain whole scenes of angiographic processes, i.e., from injection of the contrast medium to the final washout of the medium. We found the image frame from each image set that maximally presented

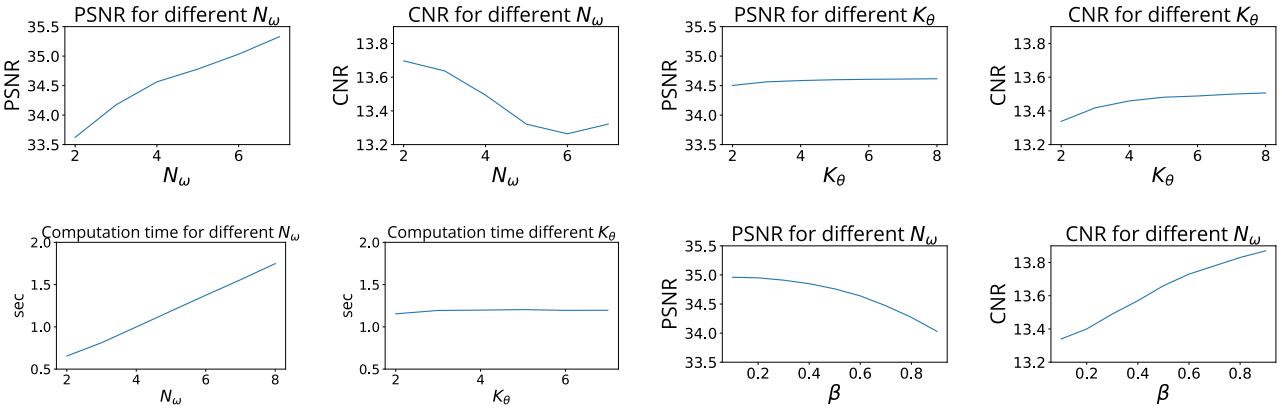

FIGURE 9. Ablation study on values of N_ω, K_θ, and β. First row: PSNR and CNR depending on N_ω, PSNR and CNR depending on K_θ, respectively. Second row: Computational complexity depending on N_ω and K_θ, PSNR and depending on β and β, respectively.

TABLE 1. PSNR and CNR results from MBS, MRF, MDP and the proposed method. Our method yields the highest performance in terms of the PSNR as well as the CNR.

	MBS [6]		MRF [7]		MDP [3]		Proposed	
No.	PSNR	CNR	PSNR	CNR	PSNR	CNR	PSNR	CNR
s-01	29.04	10.17	31.32	11.59	28.34	**11.81**	**31.82**	11.37
s-02	27.09	6.29	**28.97**	5.69	26.31	5.79	28.47	**7.11**
s-03	34.77	15.94	37.27	16.19	34.40	16.21	**38.97**	**17.04**
s-04	31.91	9.00	35.22	11.18	33.05	11.10	**37.00**	**12.72**
s-05	33.44	15.05	35.45	15.73	31.21	15.76	**35.66**	**15.78**
s-06	32.87	15.11	**34.53**	15.17	29.38	**15.36**	34.39	15.18
s-07	29.91	11.86	**32.27**	12.02	29.15	12.13	32.06	**13.28**
s-08	33.64	7.77	37.64	9.26	37.03	9.13	**39.45**	**12.47**
s-09	34.23	15.22	35.22	15.07	31.51	15.14	**35.93**	**16.08**
s-10	30.16	11.38	**39.44**	**19.42**	36.93	19.37	39.07	18.93
s-11	32.20	13.78	**34.47**	13.65	31.11	13.69	33.38	**13.86**
s-12	31.81	**13.05**	32.92	11.91	31.42	12.04	**36.50**	12.85
s-13	29.67	7.82	**32.90**	7.33	30.91	7.30	31.15	**8.77**
s-14	32.00	8.72	33.84	9.22	32.59	9.03	**37.22**	**12.13**
s-15	31.49	**10.84**	**34.24**	10.54	31.77	10.55	32.69	10.72
s-16	32.64	12.52	**37.16**	**15.80**	34.53	15.78	35.57	15.15
mean	31.68	11.53	34.55	12.49	31.85	12.51	**34.96**	**13.34**

contrasted vessels, and then chose five consecutive frames around the frame for quantitative comparison.

Table 1 compares mean PSNR and CNR results from MBS, MRF, MDP and the proposed method. The proposed method outperforms other methods for PSNR in 8 out of 16 image sets, while MRF produces the highest values in the rest of the eight sets. When comparing CNR, our method shows the best results in 10 out of 16 image sets. Among the remaining five, MBS, MRF, MDP is the best for two sets respectively. Overall, the proposed method presents the best results for both the mean PSNR and CNR values on average.

The proposed method also shows good performance regarding computational complexity. The overall computation takes 8.6, 5.2, 6.1, and 1.3 seconds for MBS, MRF, MDP and the proposed method respectively. We note the computation time for our method increases linearly with the number of levels, but it does not exceed 1.8 seconds. We provide a more detailed ablative analysis in the next section.

In sum, our method yields the highest performance concerning the PSNR, CNR as well as the computation time. These results strongly support our contribution that the proposed method effectively reduces registration errors in background regions, while maximizing contrast between background and foreground regions.

E. ABLATIVE STUDY

There are three parameters that must be determined in the proposed method: 1) the number of frequency bands for ω, which we denote as N_ω, 2) the number of orientation levels for θ, which we denote as K_θ, and 3) the parameter β which controls the similarity comparison constraint, with the range of $0 < \beta < 1$.

We first present ablative analysis on the values of N_ω and K_θ. Fig. 9(a), (b), (c) and (d) shows the average quantitative performance, measured in by both PSNR and CNR for fifteen cases. Since both N_ω and K_θ are used together to create the steerable pyramid, we compute the average values for all possible values of K_θ when computing for N_ω and vice versa. We can see that the performance increases, regarding PSNR, when increasing either the number of frequency bands N_ω or the number of orientation bands K_θ, but also that N_ω has a much more significant effect. Regarding CNR, the effect of the N_ω value is somewhat unclear. On the other hand, it is clear that increasing K_θ improves CNR on average.

We then examined the tradeoffs of increasing N_ω and K_θ by measuring the computational cost for each value. Fig. 9(c) and (d) show the average computational time, in seconds, for different values of N_ω and K_θ. It shows that the computation increases linearly with increasing N_ω, but does not depend on K_θ. This is expected since larger values of N_ω increases the number of pyramid levels of the steerable pyramid, where each level is iteratively computed. Thus, it should be noted that we can expect better DSA quality with higher N_ω, but with a slight additional computational cost. Also, it is generally safe to use a high value of K_θ for higher DSA quality.

We finally examined the cost of different β values on DSA quality. We can see that the PSNR is high and the CNR is low when β is closer to 0, meaning that only considering significant magnitude differences is better for DSA quality.

IV. CONCLUSION

We developed a novel algorithm for nonrigid deformation preserving the actual differences between images. The proposed method applies for phase-based motion compensation in the frequency domain, on filter responses obtained using complex steerable pyramids. Regions with likely changes are estimated based on the magnitude and explicitly excluded from this process to generate a deformed image which aligns motion but preserves changes. As a result, we demonstrated enhanced contrast as well as improved motion compensation quality, compared to a previous state-of-the-art registration technique.

The proposed method is also efficient and does not require a critical parameter to be tuned. Our work can be easily extended to three-dimensional applications such as computed tomography angiography or magnetic resonance angiography. It may also be applied to multi-modal registration due to the use of the frequency domain.

The major drawback of the proposed method is the limitation on the amount of motion that can be compensated. The bound of possible motion can be theoretically calculated [10], to be up to 2 to the power of $N_l - 1$, where N_l is the number of levels. In practice, however, ringing artifacts usually occur because high-frequency signals that form the object boundaries are mixed and difficult to distinguish. This issue will be addressed in our subsequent future works, e.g., by applying new approaches [28], [29] classifying signals through machine learning.

REFERENCES

[1] R. J. Radke, S. Andra, O. Al-Kofahi, and B. Roysam, "Image change detection algorithms: A systematic survey," *IEEE Trans. Image Process.*, vol. 14, no. 3, pp. 294–307, Mar. 2005.

[2] L. Alvarez, R. Deriche, T. Papadopoulo, and J. Sánchez, "Symmetrical dense optical flow estimation with occlusions detection," *Int. J. Comput. Vis.*, vol. 75, no. 3, pp. 371–385, 2007.

[3] L. Xu, J. Jia, and Y. Matsushita, "Motion detail preserving optical flow estimation," *IEEE Trans. Pattern Anal. Mach. Intell.*, vol. 34, no. 9, pp. 1744–1757, Sep. 2012.

[4] K. Englmeier, U. Fink, and T. Hilbertz, "Automated pixel shifting in digital subtraction angiography—An application of cepstral filtering," in *Computer Assisted Radiology*. Berlin, Germany: Springer, 1993, p. 795.

[5] E. H. W. Meijering, K. J. Zuiderveld, and M. A. Viergever, "Image registration for digital subtraction angiography," *Int. J. Comput. Vis.*, vol. 31, nos. 2–3, pp. 227–246, 1999.

[6] M. Nejati, S. Sadri, and R. Amirfattahi, "Nonrigid image registration in digital subtraction angiography using multilevel B-spline," *BioMed Res. Int.*, vol. 2013, Jun. 2013, Art. no. 236315.

[7] M. Sundarapandian, R. Kalpathi, and V. D. Manason, "DSA image registration using non-uniform MRF model and pivotal control points," *Comput. Med. Imag. Graph.*, vol. 37, no. 4, pp. 323–336, 2013.

[8] Y. Bentoutou, N. Taleb, M. C. El Mezouar, M. Taleb, and J. Jetto, "An invariant approach for image registration in digital subtraction angiography," *Pattern Recognit.*, vol. 35, no. 12, pp. 2853–2865, Dec. 2002.

[9] N. Wadhwa, M. Rubinstein, F. Durand, and W. T. Freeman, "Phase-based video motion processing," *ACM Trans. Graph.*, vol. 32, no. 4, p. 80, 2013.

[10] S. Meyer, O. Wang, H. Zimmer, M. Grosse, and A. Sorkine-Hornung, "Phase-based frame interpolation for video," in *Proc. IEEE Conf. Comput. Vis. Pattern Recognit.*, Jun. 2015, pp. 1410–1418.

[11] E. P. Simoncelli and W. T. Freeman, "The steerable pyramid: A flexible architecture for multi-scale derivative computation," in *Proc. ICIP*, vol. 3, 1995, pp. 444–447.

[12] M. Hemmendorff, M. T. Andersson, T. Kronander, and H. Knutsson, "Phase-based multidimensional volume registration," *IEEE Trans. Med. Imag.*, vol. 21, no. 12, pp. 1536–1543, Dec. 2002.

[13] J. Liu, B. C. Vemuri, and J. L. Marroquin, "Local frequency representations for robust multimodal image registration," *IEEE Trans. Med. Imag.*, vol. 21, no. 5, pp. 462–469, May 2002.

[14] C. Ordóñez, C. Cabo, A. Menéndez, and A. Bello, "Detection of human vital signs in hazardous environments by means of video magnification," *PLoS ONE*, vol. 13, no. 4, 2018, Art. no. e0195290.

[15] T. W. Sederberg and S. R. Parry, "Free-form deformation of solid geometric models," *ACM SIGGRAPH Comput. Graph.*, vol. 20, no. 4, 1986, pp. 151–160.

[16] N. Komodakis and G. Tziritas, "Approximate labeling via graph cuts based on linear programming," *IEEE Trans. Pattern Anal. Mach. Intell.*, vol. 29, no. 8, pp. 1436–1453, Aug. 2007.

[17] S. Klein, M. Staring, K. Murphy, M. A. Viergever, and J. P. W. Pluim, "elastix: A toolbox for intensity-based medical image registration," *IEEE Trans. Med. Imag.*, vol. 29, no. 1, pp. 196–205, Jan. 2010.

[18] B. Glocker, N. Komodakis, G. Tziritas, N. Navab, and N. Paragios, "Dense image registration through MRFs and efficient linear programming," *Med. Image Anal.*, vol. 12, no. 6, pp. 731–741, 2008.

[19] Y. Wang, Y. Yang, Z. Yang, L. Zhao, P. Wang, and W. Xu, "Occlusion aware unsupervised learning of optical flow," in *Proc. IEEE Conf. Comput. Vis. Pattern Recognit.*, Jun. 2018, pp. 4884–4893.

[20] J. Hur and S. Roth, "MirrorFlow: Exploiting symmetries in joint optical flow and occlusion estimation," in *Proc. IEEE Int. Conf. Comput. Vis.*, Oct. 2017, pp. 312–321.

[21] J.-M. Perez-Rua, T. Crivelli, P. Bouthemy, and P. Perez, "Determining occlusions from space and time image reconstructions," in *Proc. IEEE Conf. Comput. Vis. Pattern Recognit.*, Jun. 2016, pp. 1382–1391.

[22] J. Tanguay, H. K. Kim, and I. A. Cunningham, "A theoretical comparison of X-ray angiographic image quality using energy-dependent and conventional subtraction methods," *Med. Phys.*, vol. 39, no. 1, pp. 132–142, 2012.

[23] C. S. Burton, J. R. Mayo, and I. A. Cunningham, "Energy subtraction angiography is comparable to digital subtraction angiography in terms of iodine Rose SNR," *Med. Phys.*, vol. 43, no. 11, pp. 5925–5933, 2016.

[24] C. S. Burton, J. R. Mayo, and I. A. Cunningham, "Theoretical and experimental comparison of image signal and noise for dual-energy subtraction angiography and conventional X-ray angiography," *Proc. SPIE*, vol. 9412, Mar. 2015, Art. no. 941219.

[25] B. Liu *et al.*, "A vessel segmentation method for serialized cerebralvascular DSA images based on spatial feature point set of rotating coordinate system," *Comput. Methods Programs Biomed.*, vol. 161, pp. 55–72, Jul. 2018.

[26] M. Nejati and H. Pourghassem, "Multiresolution image registration in digital X-ray angiography with intensity variation modeling," *J. Med. Syst.*, vol. 38, no. 2, p. 10, 2014.

[27] T. Ohnishi, Y. Takano, H. Kato, Y. Ooka, and H. Haneishi, "Respiratory-synchronized digital subtraction angiography based on a respiratory phase matching method," *Signal, Image Video Process.*, vol. 12, no. 3, pp. 539–547, 2018.

[28] Z. Jin, G. Zhou, D. Gao, and Y. Zhang, "EEG classification using sparse Bayesian extreme learning machine for brain–computer interface," *Neural Comput. Appl.*, pp. 1–9, Oct. 2018. doi: 10.1007/s00521-018-3735-3.

[29] N. Liu, L. Wan, Y. Zhang, T. Zhou, H. Huo, and T. Fang, "Exploiting convolutional neural networks with deeply local description for remote sensing image classification," *IEEE Access*, vol. 6, pp. 11215–11228, 2018.

SOOCHAHN LEE received the B.S. and Ph.D. degrees from Seoul National University, Seoul, South Korea, in 2004 and 2011, respectively.

From 2011 to 2014, he was with the Digital Media and Communications R&D Center, Samsung Electronics, and from 2014 to 2019, he was an Assistant Professor with Soonchunhyang University, Asan, South Korea. Since 2014, he has been an Assistant Professor with the Department of Electronic Engineering, Soonchunhyang University. Since 2019, he has been an Assistant Professor with the School of Electrical Engineering, Kookmin University, Seoul. His research interests include computer vision and medical image analysis.

CHANG HO JEON received the M.S. and M.D. degrees in medicine from Seoul National University, Seoul, South Korea, in 2006 and 2016, respectively.

From 2010 to 2013, he trained and completed a fellowship at the Department of Radiology, Seoul National Bundang Hospital, Seongnam, South Korea, and completed a fellowship after his residency, from 2014 to 2015. He was an Assistant Professor with the Department of Radiology, in 2016, and since 2016, he has been an Assistant Professor with the Department of Radiology, Pusan National University Hospital, Busan, South Korea. His research interests include vascular intervention, embolotherapy, transarterial chemoembolization, angioplasty, and trauma intervention.

Dr. Jeon is a member of the Korean Medical Association, the Korean Society of Radiology, the Korean Society of Interventional Radiology, the Korean Society of Traumatology, and the Cardiovascular and Interventional Radiological Society of Europe.

LEONARD SUNWOO received the M.D., M.S., and Ph.D. degrees in medicine from Seoul National University, Seoul, South Korea, in 2006, 2014, and 2018, respectively.

From 2010 to 2014, he trained at the Department of Radiology, Seoul National University Hospital, Seoul, during his residency, where he also completed a fellowship. From 2015 to 2016, he was an Assistant Professor with the Seoul Metropolitan Government–Seoul National University Boramae Medical Center, Seoul. He has been an Associate Professor with the Department of Radiology, Seoul National University Bundang Hospital, Seongnam, South Korea, since 2016. His research interests include the machine learning and deep learning applications in medical imaging, brain tumor, and stroke imaging.

Dr. Sunwoo is a member of the Korean Society of Radiology, the Korean Society of Neuroradiology, the Korean Society of Magnetic Resonance in Medicine, the International Society for Magnetic Resonance in Medicine, and the Radiological Society of North America.

DONG YUL OH received the B.S. degree in digital information engineering from the Hankuk University of Foreign Studies, Yongin, South Korea, in 2018. He is currently pursuing the M.S. degree in bioengineering with Seoul National University, Seoul, South Korea.

In 2017, he was a Student Intern with the Music and Audio Research Group, Seoul National University. In 2018, he was a Research Intern with NAVER Webtoon Corporation, Seongnam, South Korea. Since 2017, he has been an Artificial Intelligence Researcher with the Department of Radiology, Seoul National University Bundang Hospital, Seongnam. His research interests include computer-aided diagnosis, deep-learning-based medical image analysis, and statistical validation.

KYONG JOON LEE received the M.S. and Ph.D. degrees in electrical engineering and computer science from Seoul National University, Seoul, South Korea, in 2005 and 2013, respectively.

From 2011 to 2012, he was a Research Intern with the Internet Graphics Group, Microsoft Research, Beijing, China, and the Nexus Group, Microsoft Research, Redmond, USA, during his Ph.D. degree. From 2013 to 2015, he was a Research Staff Member with the Medical System Lab, Samsung Advanced Institute of Technology, Suwon, South Korea. He was a Senior Engineer with the Medical Imaging Group, Health and Medical Equipment Division, Samsung Electronics, Seoul, from 2015 to 2016. Since 2016, he has been an Assistant Professor with the Department of Radiology, Seoul National University Bundang Hospital, Seongnam, South Korea. His research interests include medical image Analysis, computer vision, and machine learning.